Mid-wave to near-IR optoelectronic properties and epsilon-near-zero behavior in iridium-doped cadmium oxide

Angela Cleri[1], John Tomko[2], Kathleen Quiambao-Tomko[2], Mario V. Imperatore[3], Yanglin Zhu[4], J. Ryan Nolen[5], Joshua Nordlander[1], Joshua D. Caldwell[5], Zhiqiang Mao[4], Noel C. Giebink[3], Kyle P. Kelley[6], Evan Runnerstrom[7], Patrick Hopkins[2,8,9], and Jon-Paul Maria[1]

[1] Penn State University, Department of Materials Science and Engineering; [2] University of Virginia, Department of Materials Science and Engineering; [3] Penn State University, Department of Electrical Engineering; [4] Penn State University, Department of Physics; [5] Vanderbilt University, Interdisciplinary Materials Science Program; [6] Oak Ridge National Laboratory, Center for Nanophase Materials Science; [7] Army Research Office, CCDC US Army Research Laboratory, Research Triangle Park, NC 27709; [8] University of Virginia, Department of Mechanical and Aerospace Engineering; [9] University of Virginia, Department of Physics

ABSTRACT

Indium-doped cadmium oxide (In:CdO) thin films exhibit tunable epsilon-near-zero (ENZ) modal frequencies across a wide spectral range, bridging the mid-wave and near-infrared (IR). In:CdO thin films are prepared by reactive co-sputtering from metallic Cd and In targets using high-power impulse magnetron sputtering (HiPIMS) and radio frequency (RF) sputtering, respectively. Using this approach, CdO thin films with carrier concentrations ranging from 2.3×10^{19} to 4.0×10^{20} cm^{-3} and mobilities ranging from 300 to 400 $cm^2/V\cdot s$ are readily achieved. UV-VIS absorption spectra are used to measure optical bandgap, revealing a Burstein-Moss shift of 0.58 eV across the doping range investigated. Optical measurements demonstrate the tunability of near-perfect plasmonic ENZ absorption across the mid-wave and into the near-IR spectral ranges by controlling the carrier concentration through doping, while tuning the film thickness for impedance matching. In comparison to other dopants that can be introduced to HiPIMS-deposited CdO, In offers the largest range of carrier concentrations while maintaining high mobility, thus allowing for the widest accessibility of the IR spectrum of a single plasmonic material grown by sputtering.

I. INTRODUCTION

Plasmonic oscillations stand at the forefront of photonics research giving the ability to support strong light-matter interactions at sub-diffractional length scales. Recently, accessing the infrared (IR) spectral range through plasmonic resonances has stimulated interest due to phenomena including evanescent coupling, chemical sensing, hot-carrier injection, tunable absorption, high-harmonic generation, and optical characterization.[1–7]

Traditional plasmonic materials such as gold (Au) and silver (Ag) support plasmonic modes in the visible range as carrier densities are generally fixed in the 10^{22} to 10^{23} cm^{-3} range.[8] With sophisticated nanofabrication, metals can be made to host IR plasmons, like spoof plasmons in Au or Ag grid structures.[9,10] However, these materials tend to exhibit significant optical losses in the mid-wave to near-IR due to their low mobility values,[11] while the confinement of the plasmonic fields are limited due to the extremely large negative permittivities of these materials in this spectral range. While many semiconductors offer plasma frequencies in either the mid- or near-IR, currently there isn't a single material that can bridge these frequency ranges, allowing for accessibility across mid- to near-IR.[12–14]

Transparent conducting oxides (TCOs) are attractive materials for accessing IR plasmon resonance modes.[8,12] In several material systems, the carrier concentration can be tuned across ranges spanning 10^{17} to 10^{21} cm^{-3} to allow plasmonic light-matter interactions in multiple segments of the IR window.[8,12,13,15–17] Aluminum-doped zinc oxide (AlZnO) has been shown to support surface plasmon polaritons (SPPs) in the near-IR (about 1 to 3 μm wavelength range).[18] Indium tin oxide (ITO) thin film epsilon-near-zero (ENZ) frequency can be tuned between wavelengths of roughly 1 to 5 μm, and pushed further to 5 to 10 μm by fabricating nanostructures or periodic arrays.[15] However, these materials' mobilities tends to be relatively low (typically below 200 $cm^2/V{\cdot}s$), especially at lower carrier density (corresponding to longer wavelengths), resulting in relatively high optical losses.[12,13,15]

Cadmium oxide (CdO) is one of the most promising TCO candidates for low-loss mid-IR plasmonics to date resulting from its high mobilities, allowing for enhanced light-matter interactions and light confinement.[6,19,20] This was first demonstrated in 2015 by Sachet *et al*., where tunable carrier concentrations from 10^{19} to 10^{21} cm^{-3} were demonstrated in dysprosium-doped CdO (Dy:CdO) grown by molecular beam epitaxy (MBE) with peak mobilities of 500

$cm^2/V{\cdot}s$.[6] More recently, Runnerstrom *et al.* and Kelley *et al.* showed that MBE-quality doped CdO films could be prepared using reactive high-power impulse magnetron sputtering (HiPIMS).[19,20] These films have been shown to support dispersive SPP modes as well as extremely subwavelength light confinement in epsilon-near-zero (ENZ) modes.[19] ENZ modes occur in films with extreme subwavelength thicknesses ($< \lambda/50$), on the order of the skin depth, and at frequencies close to the plasma frequency, at which the dielectric constant of the film crosses through zero.[21] Various donor dopants can be employed to control the carrier concentration and tailor the plasmonic resonance at wavelengths across the mid-IR. HiPIMS-grown yttrium-doped CdO (Y:CdO) yields carrier densities up to 3.3×10^{20} cm^{-3}, but mobility values fall at densities above 2.5×10^{20} cm^{-3}.[20] Fluorine-doped CdO (F:CdO) achieves carrier concentrations only up to 1.6×10^{20} cm^{-3}, though high mobilities (300-500 $cm^2/V{\cdot}s$) are maintained across the range.[19]

In F- and Y-doped CdO, one can achieve tunable SPP and ENZ modal frequencies spanning the mid-IR, coupling to wavelengths as short as 2.8 μm and 2.4 μm, respectively.[19,20] Pushing further into the near-IR is desirable to expand the range of wavelengths accessible by this single material. The near-IR is an especially relevant range for telecommunications, spectroscopy for biomedical and pharmaceutical applications, and atmospheric sensing.[22–24] However, accessing this range requires identifying a dopant that supports higher carrier densities while maintaining high mobility values.

Indium is a promising dopant for accessing the near-IR in CdO thin films. Several reports in the literature demonstrate In:CdO thin films with carrier concentrations reaching the low-to-mid 10^{20} cm^{-3} range[25,26] and even extending to the low 10^{21} cm^{-3} range.[27] These carrier ranges may enable plasmon resonances in the near-IR. However, these high carrier densities are accompanied by relatively low mobilities (below 100 $cm^2/V{\cdot}s$), which would inhibit the plasmon quality factors.

Recently, using HiPIMS-grown In:CdO, films with high carrier densities and high mobilities (>300 $cm^2/V{\cdot}s$) have been used to support a number of interesting nanophotonics phenomena including femtosecond optical polarization switching, hybridization of SPP modes with deeply subwavelength ENZ modes, and structures supporting multiple ENZ layers.[28–30] In all cases, polaritonic oscillations approached the near-IR spectrum. In this paper we report a comprehensive study of In:CdO, demonstrating ENZ modal frequencies spanning the mid-wave IR and pushing into the near-IR and extending up to about 1.9 μm wavelength. This is achieved by reaching higher

carrier densities than have been reported for other dopants in HiPIMS-deposited CdO, while maintaining the high carrier mobilities general to this material across the whole range. Further, a 0.58 eV shift of the optical bandgap was observed with increasing carrier density across the doping range studied, and carrier density dependent thermal transport and residual resistivity ratio. These results, in concert with our recent report on the dielectric function of In:CdO,[31] offer the necessary bedrock on which future designs of IR plasmonic devices using In:CdO can be based.

II. EXPERIMENTAL PROCEDURE

In:CdO is grown on *r*-plane (012) Al_2O_3 single crystal substrates (Jiaozuo TreTrt Materials) from two-inch diameter 99.9999% pure and 99.99% pure metal Cd and In targets, respectively, using reactive HiPIMS (Starfire Industries Impulse Pulsed Power Module and Advanced Energy MDX 1.5K DC power supply) and RF plasma (Kurt J. Lesker R301 RF Power Supply) drives, respectively. HiPIMS drive conditions are 800 Hz frequency and 80 μs pulse time, producing a 1250 μs period and 6.4% duty cycle. RF power is controlled between 0 and 40 W (0 and 2 W/cm^2). Magnetrons are oriented in a sputter-down geometry with ~45° incidence angle. Substrates are adhered to a stainless steel sample holder using silver paint (Ted Pella) and heated to 400°C prior to and during deposition using a radiative sample heater. The deposition occurs in a mixed argon (20 sccm) and oxygen (14.4 sccm) environment with a total pressure of 10 mTorr. After deposition, samples are annealed in static oxygen at 635°C for 30 minutes.

Electronic properties are measured in the van der Pauw configuration using an Ecopia HMS-3000 Hall Effect measurement system with a 0.545 T magnet. X-ray reflectivity is used to measure film thickness via a PANalytical Empyrean XRD in a parallel beam geometry with a double-bounce monochromator and a parallel-plate collimator. Atomic force microscopy (AFM) images were collected using an Asylum Research MFP-3D AFM in tapping mode.

IR attenuated total reflectance (ATR-IR) spectra are collected in the Kretschmann configuration using an IR variable-angle spectroscopic ellipsometer (J. A. Woollam IR-VASE) and a right-angle CaF_2 prism to couple light into the films from the back side of the substrate. An index matching fluid (Cargille Series M, n = 1.720) is used between the prism and substrate to enhance light coupling. The UV-VIS optical properties were collected in transmission using a Perkin-Elmer Lambda 25 UV/VIS spectrometer in the 190-1100 nm wavelength range with 2 nm resolution.

Temperature dependent electrical transport measurements were collected using a standard four-probe method in a Physical Property Measurement Systems (PPMS, Quantum Design). The temperature dependence of longitudinal resistivity (ρ_{xx}) was measured between 3K and 300K.

Thermal conductivity was measured using time-domain thermoreflectance (TDTR). This optical pump-probe technique has been used extensively for determining the thermal conductivity of thin films,[32–34] including previous work on Dy:CdO films and doped/intrinsic CdO multilayer films,[6,3536] and is described in-depth elsewhere.[37,38] In this work, a 70 +/- 5 nm aluminum transducer is deposited on the CdO films, which is ideal for the two-tint TDTR system.[39] To accurately separate the intrinsic thermal conductivity of the CdO film from the thermal resistances of the Al/CdO and CdO/Al_2O_3 interfaces, the modulation frequency of the pump beam is varied from 1.05 to 8.40 MHz with an electro-optical modulator, which effectively varies the sensitivity of the TDTR thermal model to various thermophysical parameters.[40] As the pump and probe are focused to spot sizes of 23 μm and 11.5 μm, respectively, the primary source of error is due to the uncertainty in the Al transducer thickness. Note that literature values are assumed for the heat capacity of CdO in our thermal analysis.[41]

III. RESULTS AND DISCUSSION

Carrier concentration and mobility directly affect plasma frequency and quality factor of plasmonic absorption as well as other transport properties. To characterize electronic properties as a function of In content, Hall effect measurements are performed for a series of In:CdO both before and after a 30 minute anneal in static oxygen, as shown in FIG. 1a and b. The In magnetron power density is varied between 0 and 2 W/cm^2 while Cd flux is current-controlled at a constant 0.12 A, yielding an average deposition rate of ~22 nm/min. Thickness is kept constant at approximately 180 nm. At low power densities, the carrier concentration is about 2.5×10^{19} cm^{-3} and mobility is about 300 cm^2/V·s for both the as-deposited and annealed states. Very little change occurs in CdO transport properties until the In power density exceeds about 0.3 W/cm^2. Above this range both carrier density and mobility begin to increase. When the In power density reaches a threshold (in this system, 0.5 W/cm^2), the carrier density reaches 6.0×10^{19} cm^{-3} in the annealed state and the mobility peaks at ~ 400 cm^2/V·s, then experiences a small reduction to about 350 cm^2/V·s at the highest density as shown in FIG. 1b. The relationship between In content and electronic properties

can be attributed to a combination of intrinsic and extrinsic defect formation as described by the following Kröger-Vink equations.

$$\mathrm{Cd}_{\mathrm{Cd}}^{\times} + \mathrm{O}_{\mathrm{O}}^{\times} \leftrightarrow V_{\mathrm{O}}^{\cdot\cdot} + \mathrm{Cd}_{\mathrm{Cd}}^{\times} + 2\mathrm{e}' + \frac{1}{2}\mathrm{O}_2(\mathrm{g}) \quad (1)$$

$$\mathrm{In}_2\mathrm{O}_3 \overset{\mathrm{CdO}}{\longleftrightarrow} 2\mathrm{In}_{\mathrm{Cd}}^{\cdot} + 2\mathrm{O}_{\mathrm{O}}^{\times} + 2\mathrm{e}' + \frac{1}{2}\mathrm{O}_2(\mathrm{g}) \quad (2)$$

CdO tends toward *n*-type conductivity due to its high propensity for oxygen loss, which manifests in anion vacancies compensated by free electrons, as shown by Eq. 1. High temperatures and low oxygen pressures drive this reaction to the products side. Indium incorporation on Cd sites, at least at low-to-medium concentrations, is also electron compensated as shown in Eq. 2. These two defect equilibrium reactions occur simultaneously, interacting with each other and their environments. For the situation of strong In-doping one expects a large electron concentration that is pinned by composition via the relative Cd and In fluxes from the individual sputter cathodes. Since n_e is also on the products side of Eq. 1, Le Chatlier's principles suggests that the reaction will shift to the reactants side, thereby suppressing oxygen vacancy formation. Oxygen vacancies produce a large strain field (confirmed by density functional theory (DFT) calculations[6]) and are doubly charged (presenting a four-fold higher ionized impurity cross-section than singly charged defects), so reducing $[V_0^{\cdot\cdot}]$ through donor doping strongly reduces carrier scattering and boosts mobility, despite the presence of In impurites.[42] A modest reduction in the mobility does occur at the highest In levels where we anticipate electron-electron scattering and/or the formation of $V_{Cd}^{''}$ as the preferred compensating species, as we discuss below.

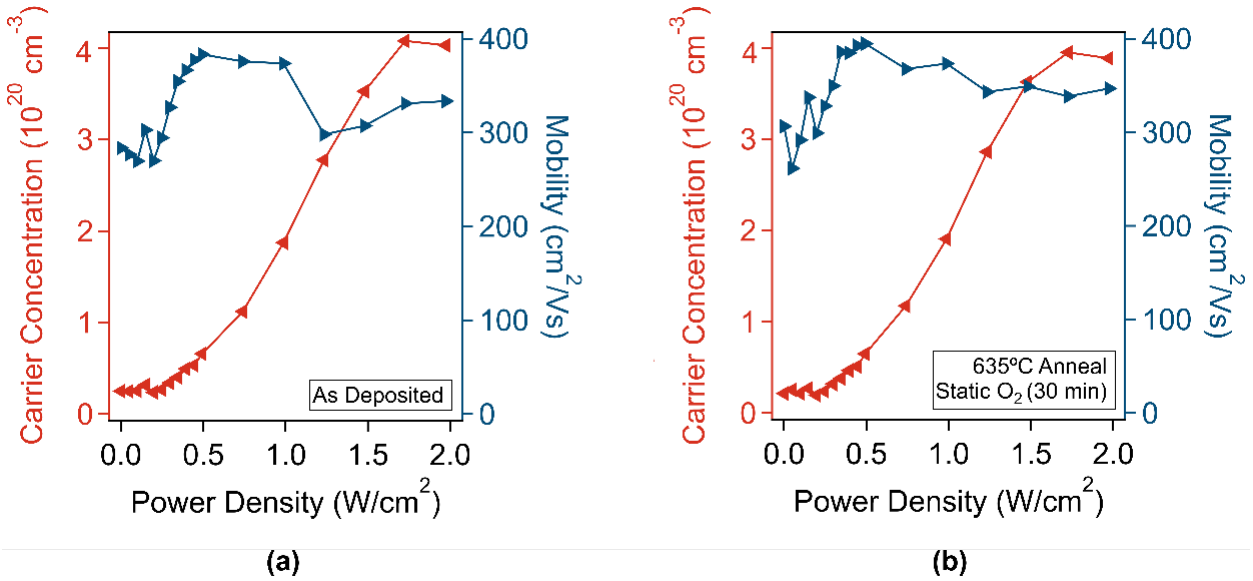

FIG. 1. Electronic properties as a function of power density in In:CdO thin films (a) as-deposited and (b) after a 30 minute anneal at 635°C in static oxygen.

Similar donor doping effects have been reported for Dy, Y, and F incorporation in CdO.[6,19,20] These dopants nonetheless cause a significant drop in mobility high carrier concentrations. As we show here, however, In doping allows mobilities ≥350 cm^2/V·s, even in samples with n_e as high as 4×10^{20} cm^{-3}. Kelley *et al*. and Runnerstron *et al.* found maximum carrier density values (while retaining high mobility) of 2.5×10^{20} cm^{-3} and 1.6×10^{20} cm^{-3} for Y and F donor doping, respectively, in HiPIMS-deposited CdO.[19,20] The comparison between Y- and In-doping is particularly interesting because both cases involve the same HiPIMS/RF reactive co-sputtering process, while F-doping involved introducing CF_4 gas. Despite not maintaining high mobilities at as high carrier densities, Y-doping exhibits a higher peak mobility (> 400 cm^2/V·s) than realized through In-doping. Typically, such differences in dopant behavior can be attributed to differences in ionic radii between the dopant and host atoms, as large differences may produce strong scattering sites. Based on ionic radii differences, Y^{3+} and In^{3+} should locally produce 4.6% and 13.8% tensile strains if substituted for Cd^{2+}, respectively.[43] The higher peak mobility at modest Y concentrations may be attributed to lower local strain.

To explain the sustained high mobility values in high carrier density In:CdO, we speculate that the much smaller electronegativity difference between In and Cd ($\Delta E < 0.1$) in comparison to that of

Y and Cd ($\Delta E \sim 0.4$) is the predominant influence. In our working model, the similar ionicity of the In-O bond allows high incorporation without phase separation, and electrostatic compensation primarily through donor creation. Better hybridization of In-donor and CdO-conduction-band-edge states is likely the underpinning cause.

This reasoning may also support the high peak mobility observation in Y:CdO. It is possible that Y incorporation at sufficiently low concentrations has a smaller influence on the conduction band minimum due to the higher electronegativity difference as well as poor hybridization between the *d* orbitals of Y and the *s* and *p* orbitals of Cd, limiting ionized impurity scattering.[44,45] This, coupled with minimal tensile strain due to similar lattice constants may allow for higher peak mobility at low Y concentrations. However, it should be noted that these higher mobility values were only observed at carrier densities well below those achieved with In and that the characteristic sharp drop off in mobility is observed at higher carrier concentrations. At Y concentrations exceeding ~ 2×10^{20} cm^{-3}, x-ray line widths broaden and mobility falls suggesting a possible solubility limit and formation of structural defects that reduce mobility faster than in the case of In incorporation at higher carrier densities. Yang, *et al.* also witnessed this effect in Y:CdO, and attributed the limited carrier concentration and mobility decrease to lower Y solubility in the CdO lattice as well as the tendency of Y *d*-band states to perturb the conduction band minimum of Y:CdO at higher concentrations.[44]

To investigate the slight mobility drop with increasing In content observed in FIG. 1b, we first performed X-ray diffraction analysis to explore possible crystallographic origins. Sets of $\theta - 2\theta$ and ω patterns are shown in FIG. 2a and FIG. 2b, respectively, for the post-anneal In:CdO doping series presented in FIG. 1b. FWHM for $\theta - 2\theta$ scans are nearly identical. The (002) peak indicates a rocksalt structure; no other peaks are present in any films suggesting phase purity. There is little to no shift in this peak with increasing carrier density, showing that epitaxy, phase purity, and out-of-plane lattice constant do not change significantly with doping. A narrow 2θ range is shown such that peak similarities are evident. Wide angle scans are available in the supplemental material. The FWHM for the ω scans in FIG. 2b exhibit modest broadening (up to about 0.5°) at higher In levels indicating stronger out-of-plane mosaicity, which may contribute to the slight drop in mobility at these higher carrier densities. Then, the FWHM decreases again at the highest doping level. The FWHM values are plotted in the supplemental material. This result can be compared to

ω scans of Y:CdO,[20] which demonstrate substantial broadening (FWHM > 1.2 degrees) at high dopant densities accompanied by a significant drop in mobility. This supports the claim that In is more easily soluble in CdO than Y, resulting in improved crystallinity and higher mobility at higher carrier densities. The data provided from this sample series is typical of heteroepitaxial In:CdO films on r-plane Al_2O_3 with a (001) growth habit, grown under similar conditions with similar transport properties. While it is nearly impossible to reproduce identical deposition conditions, and by extension identical data, general trends reported here are reproducible.

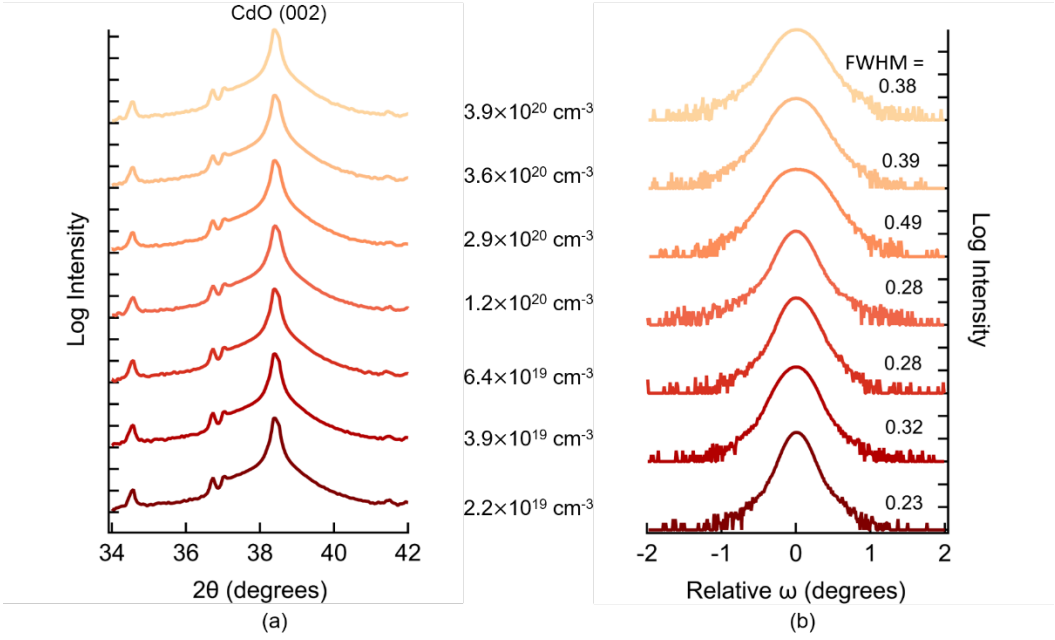

FIG. 2. (a) 2θ-ω XRD scans for heteroepitaxial post-anneal In:CdO grown on r-plane Al_2O_3 with varying In content. (b) ω rocking curves for the same set of films. FWHM values are annotated for each rocking curve.

To assess film surface microstructure, atomic force microscopy (AFM) was used for three annealed films representing low, medium, and high dopant levels. There is an apparent change from step-and-terrace growth to screw dislocation-mediated growth at higher doping levels. The images show a grainy morphology for the low-doped case with average feature sizes initially around 100 nm, a transition to smaller, but still grainy features in the medium-doped sample, and then transition to a faceted morphology at the highest doping content. We speculate that this transition originates from the well-reported surfactant effect that often accompanies In-incorporation in nitride and oxide growth.[46–49] Baldini *et al.*, reported that In acts as a surfactant,

enhancing the surface diffusion length and driving improved surface morphology of $(Ga_{1-x}In_x)_2O_3$.[49] A longer surface diffusion length is consistent with the smoother films (that express the step-and-terrace morphology of the underlying *r*-plane sapphire) at medium doping, and then the 90° faceting consistent with the 001-oriented rocksalt habit at the highest doping. For Y-doped CdO, Kelley *et al.* reported consistent step-and-terrace growth with a monotonic decrease in grain size at higher dopant levels accompanied by a significant drop in mobility.[20] It is possible that a surfactant effect-induced morphology transition from grainy to step-and-terrace at high In concentrations is important to sustaining the high mobility values in this heavily doped region, and to cap – and potentially reduce – film mosaicity in the same composition space.

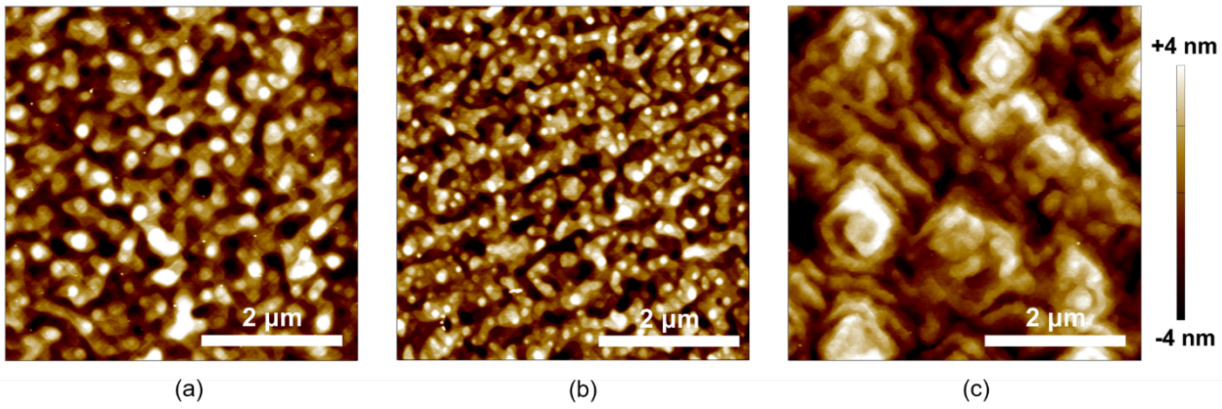

FIG. 3. AFM height retrace images of post-anneal In:CdO thin films with carrier concentrations of (a) 2.7×10^{19} cm^{-3}, (b) 1.2×10^{20} cm^{-3}, and (c) 3.9×10^{20} cm^{-3}.

A plateau in carrier concentration is observed in annealed films in FIG. 1b around 4×10^{20} cm^{-3} for the highest In fluxes where additional In does not produce more carriers. This limit persists even at In power densities beyond 2.0 W/cm^{-2}. We speculate that high doping pushes the Fermi energy so far into the conduction band that the energy cost of an electronically compensated $In_{Cd}^{\bullet}$ is no longer the lowest value for the available options. It is likely in this case that $V_{Cd}^{''}$ are easier to form as suggested in the calculations of Sachet *et al.*[6] This mechanism is consistent with the mobility drop that accompanies the carrier plateau, which would be expected from a growing population of divalent metal vacancy scattering centers. The transition from electronic to ionic compensation will be a function of the Cd chemical potential, which can in principle be tuned to shift the transition to higher carrier densities.

We evaluate this hypothesis by preparing CdO thin films at lower temperatures (200°C) to minimize Cd volatility, and increasing Cd flux to drive more Cd into the film while proportionally increasing In flux to maintain high In incorporation – measures that should shift the defect equilibrium to conditions of maximum electronic carriers with minimum metal vacancies. Both of these were performed in films about 100 nm thick, and boosted carrier density to $\sim 5\times10^{20}$ cm^{-3}.

To gain further insight into In-doping, residual resistivity ratio (RRR, ρ_{300K}/ρ_{3K}) is determined from measuring temperature-dependent longitudinal resistivity of annealed In:CdO films using a standard four-point-probe method in a PPMS. At lower temperatures, resistivity decreases due to suppressed electron-phonon scattering, resulting in RRR values greater than 1. Doping introduces more impurities into the system which is reflected by the increased RRR values with carrier concentration. Raw resistivity vs. temperature data is presented in the supplemental material. To more directly observe phonon behavior in In:CdO, room temperature thermal conductivities are measured by TDTR as shown in FIG. 4. The lattice (κ_l) and electronic (κ_e) contributions of the thermal conductivity are calculated using the Wiedemann-Franz law. These calculations account for variability in the Lorenz number in degenerate semiconductors with increased doping.[50–52]As more impurities are introduced to the system with increased doping, phonon-ion and phonon-electron scattering increase. Therefore, phonons cannot transport heat as well, causing a decrease in κ_l, which is calculated by $\kappa_{total} = \kappa_e + \kappa_l$ (shown in the supplemental material). Consequently, the thermal conductivity becomes dominated by its electronic contribution, thus the increase in κ_e. The increased phonon-electron scattering also explains the increase in RRR with doping. The increase of RRR and thermal conductivity (κ_{total}) with doping is consistent with trends presented by Sachet et al. for Dy:CdO in this carrier density range.[6]

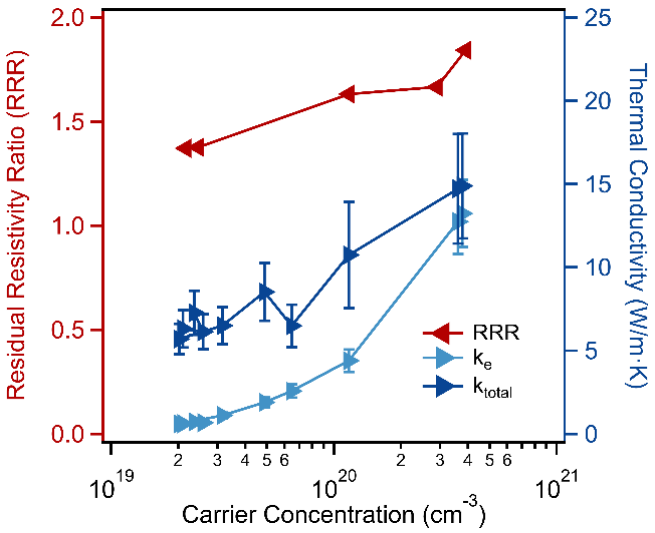

FIG. 4. Residual resistivity ratio (RRR, ρ_{300K}/ρ_{3K}), out-of-plane thermal conductivity (κ_{total}), and electronic contribution of thermal conductivity (κ_e), for annealed In:CdO films.

The degenerate nature of CdO thin films across a broad doping window motivates the possibility of a Burstein-Moss shift as the Fermi energy is pushed further into the conduction band.[44,53,54] Transmittance spectra in the UV-VIS spectral range confirm this blueshift in optical band gap with increasing doping concentration as shown by the Tauc plot in FIG. 5. Using a direct band gap model for CdO[55] and extrapolating linear fits of each data set to the abscissa indicates a Burstein-Moss shift of approximately 0.58 eV upon increasing the carrier concentration to 5.0×10^{20} cm^{-3}. Full range transmittance spectra, details of the fitting procedure, and a discussion of the optical band gap calculation are available in the supplemental material.

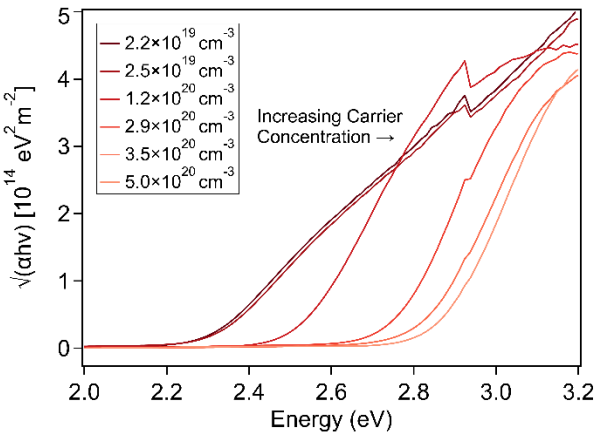

FIG. 5. Tauc plots from UV-VIS transmission data for annealed In:CdO films, showing a shift in the optical absorption threshold with increased doping. The sharp feature around 2.9 eV occurs due to a filter switch in the instrument.

Table I. Hall data and bandgap values for samples indicated in FIG. 5.

Sample	Carrier concentration (cm^{-3})	Mobility ($cm^2/V{\cdot}s$)	Bandgap (eV)	Standard Deviation (eV)
a	2.2×10^{19}	298	2.28	0.002
b	2.5×10^{19}	315	2.29	0.002
c	1.2×10^{20}	365	2.51	0.009
d	2.9×10^{20}	331	2.73	0.009
e	3.5×10^{20}	334	2.81	0.009
f	5.0×10^{20}	326	2.86	0.007

The ability to sustain high mobility values in In-doped CdO thin films from 2×10^{19} through 5×10^{20} cm^{-3} enables one to tailor the bulk plasma frequency and thus the ENZ modal frequency over a wavelength range capturing the entire mid-IR and pushing into the near-IR, while the ability to retain a smooth morphology over a thickness range spanning 10's to 100's of nanometers allows

one to engineer the perfect absorbing ENZ condition. Under the assumption that CdO films behave as Drude metals, the frequency-dependent dielectric function in the mid- to near-IR is given as

$$\varepsilon(\omega) = \varepsilon_\infty - \frac{\omega_p^2}{\omega^2 - i\omega\Gamma} \tag{3}$$

where ε_∞ is the high-frequency dielectric constant, Γ is the damping rate, and $\omega_p = \sqrt{ne^2/m^*\varepsilon_0}$ is the plasma frequency.[56] CdO thin films can support both SPP and ENZ modes.[30] Here we use ENZ modes to demonstrate plasma frequency tunability, as they can be achieved with lower film thickness and are weakly dependent on incident angle, allowing for simpler fabrication and measurements. From Eq. 3, the frequency at which an ENZ mode is supported can be approximated as[13]

$$\omega_{ENZ} \approx \sqrt{\frac{\omega_p^2}{\varepsilon_\infty} - \Gamma^2} \tag{4}$$

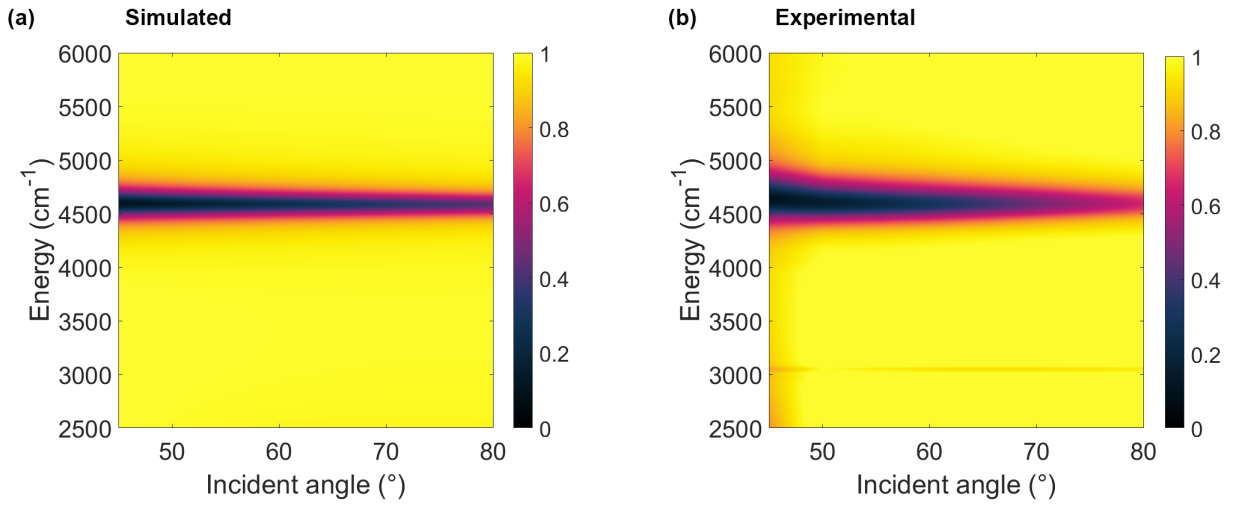

FIG. 6. (a) Simulated and (b) experimental reflectometry maps of ENZ modes in 29 nm In:CdO sample with $n = 2.7 \times 10^{20} cm^{-3}$ and $\mu = 281\ cm^2/V \cdot s$.

To explore our access to mid- and near-IR ENZ modes, a MATLAB script discussed in previous work[29,30] that employs the transfer matrix method (TMM) is used to simulate combinations of carrier density and thickness that would produce ENZ perfect absorbers at various wavelengths. These calculations assumed an effective mass of 0.21 and a high-frequency permittivity of 5.3, as

reported in the literature.[55,58] These simulated results guide fabrication of a In:CdO thin film series supporting ENZ modes spanning the entire mid-IR and pushing into the near-IR up to wavelengths of about 1.9 μm. These simulations provide a rather accurate prediction of the dispersion curve of the ENZ layer (FIG. 6). IR optical spectra are measured by ATR-IR at a 50-degree incident angle using a right-angle CaF_2 prism and an IR-VASE. Normalized ATR-IR spectra for these films are shown in FIG. 7, plotted as the ratio of *p*- to *s*-polarized light (R_p/R_s). The thickness, electrical, and optical data are summarized in TABLE II. Percent absorption is determined by $1 - R_p/R_s$ (non-normalized) for the peak minimum in each curve. Extinction peak FWHM is calculated using a Lorentzian fit for each curve. Here we demonstrate sharp absorption features with peak widths as low as 226 cm^{-1} and Q factors (ratio of peak energy to peak width) as high as 14.3.

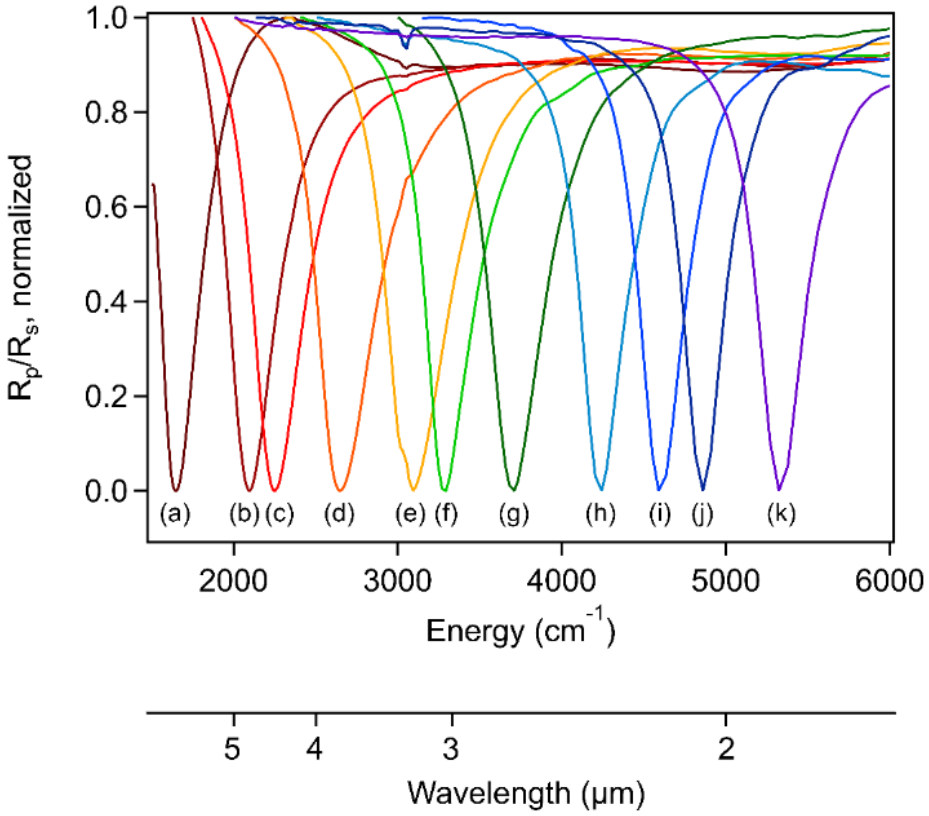

FIG. 7. Normalized experimental ATR-IR curves for In:CdO at various doping levels at a 50-degree incident angle.

TABLE II. Thickness, electrical properties, and optical properties for samples indicated in the ATR-IR curves in FIG. 5.

Sample	Thickness (nm)	Carrier Concentration (cm^{-3})	Mobility ($cm^2/V{\cdot}s$)	Extinction Peak Position	Extinction Peak FWHM	Percent Absorption	Q
a	181	3.193×10^{19}	350	1651 cm^{-1} 6.057 μm	226 cm^{-1} 818 nm	75	7.4
b	135	4.992×10^{19}	383	2098 cm^{-1} 4.766 μm	252 cm^{-1} 562 nm	71	8.4
c	133	5.748×10^{19}	388	2253 cm^{-1} 4.440 μm	321 cm^{-1} 445 nm	70	8.4
d	93	8.303×10^{19}	378	2646 cm^{-1} 3.779 μm	353 cm^{-1} 443 nm	60	8.0
e	72	1.163×10^{20}	346	3094 cm^{-1} 3.232 μm	467 cm^{-1} 477 nm	63	6.7
f	40	1.317×10^{20}	319	3294 cm^{-1} 3.036 μm	281 cm^{-1} 256 nm	59	11.8
g	38	1.606×10^{20}	269	3711 cm^{-1} 2.695 μm	362 cm^{-1} 261nm	54	10.3
h	29	2.158×10^{20}	284	4243 cm^{-1} 2.357 μm	403 cm^{-1} 222 nm	77	10.6
i	29	2.690×10^{20}	281	4590 cm^{-1} 2.179 μm	378 cm^{-1} 177 nm	85	12.2
j	24	2.969×10^{20}	291	4860 cm^{-1} 2.058 μm	341 cm^{-1} 144 nm	80	14.3
k	22	3.920×10^{20}	275	5323 cm^{-1} 1.879 μm	385 cm^{-1} 135 nm	69	13.9

IV. CONCLUSIONS

We have demonstrated that In is a viable dopant for CdO as a tunable plasmonic material, allowing for broad accessibility of the IR spectrum (through the midwave-IR and into the near-IR) via low-loss ENZ polaritons. By controlling deposition time and power density of the In dopant magnetron during deposition, we can control thickness and carrier density, allowing for engineering of plasmon modes such as perfect absorber ENZ layers that span 6 μm to 1.9 μm. The high mobilities realized across a wide range of carrier densities allow for strong plasmonic absorption and high Q factors. $\theta - 2\theta$ and ω XRD curves indicate phase purity across a broad In doping range and a slight maxima in out-of-plane mosaicity at intermediate dopant concentrations. AFM shows changes to a smoother morphology at higher doping, with a change in growth habit from step-and-terrace growth to screw dislocation-mediated growth. Comparison of ω rocking curves and AFM

data between In:CdO and Y:CdO films complement the observed higher mobility at higher carrier densities in In:CdO. RRR values from low temperature resistivity measurements and thermal conductivity from TDTR measurements over a range of carrier densities show that phonon-phonon and phonon-electron scattering increase with doping, consistent with trends previously shown in CdO.[6,35] UV-VIS transmission spectroscopy demonstrates the Burstein-Moss shift present with increased doping, as the Fermi level is pushed further into the conduction band. This work, in addition to our previous study of the dielectric function of In:CdO[31], provide a comprehensive review of the effects of In doping in CdO, paving the way for future IR plasmonic device design using In:CdO.

V. ACKNOWLEDGEMENTS

We gratefully acknowledge support from Office of Naval Research (ONR) Grant No. N00012-18-1-2107 and Army Research Office (ARO) Grant No. W911NF-16-1-0406. We also received support from the Department of Defense (DoD) through the National Defense Science and Engineering Graduate (NDSEG) Fellowship Program. K.P.K acknowledges support from the Center for Nanophase Materials Sciences, which is a U.S. Department of Energy (DOE) Office of Science User Facility. Z.Q.M. acknowledges support from the U.S. National Science Foundation (NSF) under Grant No. DMR1707502. This work was also supported in part by the NSF I/UCRC on Multi-Functional Integrated System Technology (MIST) Center; IIP-1439644, IIP-1439680, IIP1738752, IIP-1939009, IIP-1939050, and IIP-1939012.

VI. REFERENCES

1. Stanley R. Plasmonics in the mid-infrared. *Nat Photonics Lond*. 2012;6(7):409-411. doi:http://dx.doi.org.ezaccess.libraries.psu.edu/10.1038/nphoton.2012.161

2. Caldwell JD, Glembocki O, Bezares FJ, et al. Plasmonic Nanopillar Arrays for Large-Area, High-Enhancement Surface-Enhanced Raman Scattering Sensors. *ACS Nano*. 2011;5(5):4046-4055. doi:10.1021/nn200636t

3. Rodrigo D, Limaj O, Janner D, et al. Mid-infrared plasmonic biosensing with graphene. *Science*. 2015;349(6244):165-168. doi:10.1126/science.aab2051

4. Coe JV, Rodriguez KR, Teeters-Kennedy S, et al. Metal Films with Arrays of Tiny Holes: Spectroscopy with Infrared Plasmonic Scaffolding. *J Phys Chem C*. 2007;111(47):17459-17472. doi:10.1021/jp072909a

5. Lal S, Link S, Halas NJ. Nano-optics from sensing to waveguiding. *Nat Photonics Lond*. 2007;1(11):641-648. doi:http://dx.doi.org.ezaccess.libraries.psu.edu/10.1038/nphoton.2007.223

6. Sachet E, Shelton CT, Harris JS, et al. Dysprosium-doped cadmium oxide as a gateway material for mid-infrared plasmonics. *Nat Mater*. 2015;14(4):414-420. doi:10.1038/nmat4203

7. Navarro-Cia M, Maier SA. Broad-Band Near-Infrared Plasmonic Nanoantennas for Higher Harmonic Generation. *ACS Nano*. 2012;6(4):3537-3544. doi:10.1021/nn300565x

8. Naik GV, Shalaev VM, Boltasseva A. Alternative Plasmonic Materials: Beyond Gold and Silver. *Adv Mater*. 2013;25(24):3264-3294. doi:10.1002/adma.201205076

9. Pendry JB. Mimicking Surface Plasmons with Structured Surfaces. *Science*. 2004;305(5685):847-848. doi:10.1126/science.1098999

10. Sharac N, Giles AJ, Perkins K, et al. Implementation of plasmonic band structure to understand polariton hybridization within metamaterials. *Opt Express*. 2018;26(22):29363-29374. doi:10.1364/OE.26.029363

11. West P r., Ishii S, Naik G v., Emani N k., Shalaev V m., Boltasseva A. Searching for better plasmonic materials. *Laser Photonics Rev*. 2010;4(6):795-808. doi:10.1002/lpor.200900055

12. Zhong Y, Malagari SD, Hamilton T, Wasserman DM. Review of mid-infrared plasmonic materials. *J Nanophotonics*. 2015;9(1):093791. doi:10.1117/1.JNP.9.093791

13. Naik GV, Liu J, Kildishev AV, Shalaev VM, Boltasseva A. Demonstration of Al:ZnO as a plasmonic component for near-infrared metamaterials. *Proc Natl Acad Sci*. 2012;109(23):8834-8838. doi:10.1073/pnas.1121517109

14. Naik GV, Schroeder JL, Ni X, Kildishev AV, Sands TD, Boltasseva A. Titanium nitride as a plasmonic material for visible and near-infrared wavelengths. *Opt Mater Express*. 2012;2(4):478-489. doi:10.1364/OME.2.000478

15. Wang Y, Overvig AC, Shrestha S, et al. Tunability of indium tin oxide materials for mid-infrared plasmonics applications. *Opt Mater Express*. 2017;7(8). doi:10.1364/OME.7.002727

16. Franzen S. Surface Plasmon Polaritons and Screened Plasma Absorption in Indium Tin Oxide Compared to Silver and Gold. *J Phys Chem C*. 2008;112(15):6027-6032. doi:10.1021/jp7097813

17. Rhodes C, Franzen S, Maria J-P, et al. Surface plasmon resonance in conducting metal oxides. *J Appl Phys*. 2006;100(5):054905. doi:10.1063/1.2222070

18. Calzolari A, Ruini A, Catellani A. Transparent Conductive Oxides as Near-IR Plasmonic Materials: The Case of Al-Doped ZnO Derivatives. *ACS Photonics*. 2014;1(8):703-709. doi:10.1021/ph500118y

19. Runnerstrom EL, Kelley KP, Sachet E, Shelton CT, Maria J-P. Epsilon-near-Zero Modes and Surface Plasmon Resonance in Fluorine-Doped Cadmium Oxide Thin Films. *ACS Photonics*. 2017;4(8):1885-1892. doi:10.1021/acsphotonics.7b00429

20. Kelley KP, Sachet E, Shelton CT, Maria J-P. High mobility yttrium doped cadmium oxide thin films. *APL Mater*. 2017;5(7):076105. doi:10.1063/1.4993799

21. Campione S, Brener I, Marquier F. Theory of epsilon-near-zero modes in ultrathin films. *Phys Rev B*. 2015;91(12):121408. doi:10.1103/PhysRevB.91.121408

22. Dempsey RJ, Davis DG, Buice RG, Lodder RA. Biological and Medical Applications of Near-Infrared Spectrometry. *Appl Spectrosc*. 1996;50(2):18A-34A. doi:10.1366/0003702963906537

23. Shen C, Loas G, Srebro-Hooper M, et al. Iron Alkynyl Helicenes: Redox-Triggered Chiroptical Tuning in the IR and Near-IR Spectral Regions and Suitable for Telecommunications Applications. *Angew Chem Int Ed*. 2016;55(28):8062-8066. doi:10.1002/anie.201601633

24. Yang Z, Toon GC, Margolis JS, Wennberg PO. Atmospheric CO2 retrieved from ground-based near IR solar spectra. *Geophys Res Lett*. 2002;29(9):53-1-53-54. doi:10.1029/2001GL014537

25. Wang A, Babcock JR, Edleman NL, et al. Indium-cadmium-oxide films having exceptional electrical conductivity and optical transparency: Clues for optimizing transparent conductors. *Proc Natl Acad Sci*. 2001;98(13):7113-7116. doi:10.1073/pnas.121188298

26. Flores MA, Castanedo R, Torres G, Zelaya O. Optical, electrical and structural properties of indium-doped cadmium oxide films obtained by the sol–gel technique. *Sol Energy Mater Sol Cells*. 2009;93(1):28-32. doi:10.1016/j.solmat.2008.02.006

27. Zhu Y, Mendelsberg RJ, Zhu J, Han J, Anders A. Transparent and conductive indium doped cadmium oxide thin films prepared by pulsed filtered cathodic arc deposition. *Appl Surf Sci*. 2013;265:738-744. doi:10.1016/j.apsusc.2012.11.096

28. Yang Y, Kelley K, Sachet E, et al. Femtosecond optical polarization switching using a cadmium oxide-based perfect absorber. *Nat Photonics*. 2017;11(6):390-395. doi:10.1038/nphoton.2017.64

29. Kelley KP, Runnerstrom EL, Sachet E, et al. Multiple Epsilon-Near-Zero Resonances in Multilayered Cadmium Oxide: Designing Metamaterial-Like Optical Properties in Monolithic Materials. *ACS Photonics*. Published online April 18, 2019:acsphotonics.9b00367. doi:10.1021/acsphotonics.9b00367

30. Runnerstrom EL, Kelley KP, Folland TG, et al. Polaritonic Hybrid-Epsilon-near-Zero Modes: Beating the Plasmonic Confinement vs Propagation-Length Trade-Off with Doped Cadmium Oxide Bilayers. *Nano Lett*. 2019;19(2):948-957. doi:10.1021/acs.nanolett.8b04182

31. Nolen JR, Runnerstrom EL, Kelley KP, et al. Ultraviolet to far-infrared dielectric function of n -doped cadmium oxide thin films. *Phys Rev Mater*. 2020;4(2):025202. doi:10.1103/PhysRevMaterials.4.025202

32. Jiang P, Qian X, Yang R. Tutorial: Time-domain thermoreflectance (TDTR) for thermal property characterization of bulk and thin film materials. *J Appl Phys*. 2018;124(16):161103. doi:10.1063/1.5046944

33. Cheaito R, Duda JC, Beechem TE, et al. Experimental Investigation of Size Effects on the Thermal Conductivity of Silicon-Germanium Alloy Thin Films. *Phys Rev Lett*. 2012;109(19):195901. doi:10.1103/PhysRevLett.109.195901

34. Chiritescu C, Cahill DG, Nguyen N, et al. Ultralow Thermal Conductivity in Disordered, Layered WSe_2 Crystals. *Science*. 2007;315(5810):351-353.

35. Donovan BF, Sachet E, Maria J-P, Hopkins PE. Interplay between mass-impurity and vacancy phonon scattering effects on the thermal conductivity of doped cadmium oxide. *Appl Phys Lett*. 2016;108(2):021901. doi:10.1063/1.4939652

36. Radue E, Runnerstrom EL, Kelley KP, et al. Charge confinement and thermal transport processes in modulation-doped epitaxial crystals lacking lattice interfaces. *Phys Rev Mater*. 2019;3(3):032201. doi:10.1103/PhysRevMaterials.3.032201

37. Schmidt AJ, Chen X, Chen G. Pulse accumulation, radial heat conduction, and anisotropic thermal conductivity in pump-probe transient thermoreflectance. *Rev Sci Instrum*. 2008;79(11):114902. doi:10.1063/1.3006335

38. Cahill DG. Analysis of heat flow in layered structures for time-domain thermoreflectance. *Rev Sci Instrum*. 2004;75(12):5119-5122. doi:10.1063/1.1819431

39. Kang K, Koh YK, Chiritescu C, Zheng X, Cahill DG. Two-tint pump-probe measurements using a femtosecond laser oscillator and sharp-edged optical filters. *Rev Sci Instrum*. 2008;79(11):114901. doi:10.1063/1.3020759

40. Jiang P, Huang B, Koh YK. Accurate measurements of cross-plane thermal conductivity of thin films by dual-frequency time-domain thermoreflectance (TDTR). *Rev Sci Instrum*. 2016;87(7):075101. doi:10.1063/1.4954969

41. Madelung O, Rössler U, Schulz M. Cadmium oxide (CdO) debye temperature, heat capacity, melting point, density. In: *Group III Condensed Matter*. Vol 41B. ; 1999:1-3.

42. Kelley KP. Mid-Infrared Plasmonics in Cadmium Oxide Thin Films. Published online 2018.

43. Trolier-McKinstry S, Newnham RE. *Materials Engineering: Bonding, Structure, and Structure-Property Relationships*. Cambridge University Press; 2017.

44. Yang Y, Jin S, Medvedeva JE, et al. CdO as the Archetypical Transparent Conducting Oxide. Systematics of Dopant Ionic Radius and Electronic Structure Effects on Charge Transport and Band Structure. *J Am Chem Soc*. 2005;127(24):8796-8804. doi:10.1021/ja051272a

45. Runnerstrom EL, Bergerud A, Agrawal A, et al. Defect Engineering in Plasmonic Metal Oxide Nanocrystals. *Nano Lett*. 2016;16(5):3390-3398. doi:10.1021/acs.nanolett.6b01171

46. Nicolay S, Feltin E, Carlin J-F, et al. Indium surfactant effect on AlN/GaN heterostructures grown by metal-organic vapor-phase epitaxy: Applications to intersubband transitions. *Appl Phys Lett*. 2006;88(15):151902. doi:10.1063/1.2186971

47. Keller S, Heikman S, Ben-Yaacov I, Shen L, DenBaars SP, Mishra UK. Indium-surfactant-assisted growth of high-mobility AlN/GaN multilayer structures by metalorganic chemical vapor deposition. :4.

48. Voigtländer B, Zinner A, Weber T, Bonzel HP. Modification of growth kinetics in surfactant-mediated epitaxy. *Phys Rev B*. 1995;51(12):7583-7591. doi:10.1103/PhysRevB.51.7583

49. Baldini M, Albrecht M, Gogova D, Schewski R, Wagner G. Effect of indium as a surfactant in $(Ga_{1-x}In_x)_2O_3$ epitaxial growth on β-Ga_2O_3 by metal organic vapour phase epitaxy. *Semicond Sci Technol*. 2015;30(2):024013. doi:10.1088/0268-1242/30/2/024013

50. Minnich AJ, Dresselhaus MS, Ren ZF, Chen G. Bulk nanostructured thermoelectric materials: current research and future prospects. *Energy Environ Sci*. 2009;2(5):466. doi:10.1039/b822664b

51. Pichanusakorn P, Bandaru P. Nanostructured thermoelectrics. *Mater Sci Eng R Rep*. 2010;67(2-4):19-63. doi:10.1016/j.mser.2009.10.001

52. Makinson REB. The thermal conductivity of metals. :24.

53. Kumaravel R, Ramamurthi K, Krishnakumar V. Effect of indium doping in CdO thin films prepared by spray pyrolysis technique. *J Phys Chem Solids*. 2010;71(11):1545-1549. doi:10.1016/j.jpcs.2010.07.021

54. Ueda N, Maeda H, Hosono H, Kawazoe H. Band-gap widening of CdO thin films. *J Appl Phys*. 1998;84(11):6174-6177. doi:10.1063/1.368933

55. Burbano M, Scanlon DO, Watson GW. Sources of Conductivity and Doping Limits in CdO from Hybrid Density Functional Theory. *J Am Chem Soc*. 2011;133(38):15065-15072. doi:10.1021/ja204639y

56. Maier SA. *Plasmonics: Fundamentals and Applications*. Springer US; 2007. doi:10.1007/0-387-37825-1

57. Campione S, Wendt JR, Keeler GA, Luk TS. Near-Infrared Strong Coupling between Metamaterials and Epsilon-near-Zero Modes in Degenerately Doped Semiconductor Nanolayers. *ACS Photonics*. 2016;3(2):293-297. doi:10.1021/acsphotonics.5b00663

58. Liu CP, Foo Y, Kamruzzaman M, et al. Effects of Free Carriers on the Optical Properties of Doped CdO for Full-Spectrum Photovoltaics. *Phys Rev Appl*. 2016;6(6):064018. doi:10.1103/PhysRevApplied.6.064018